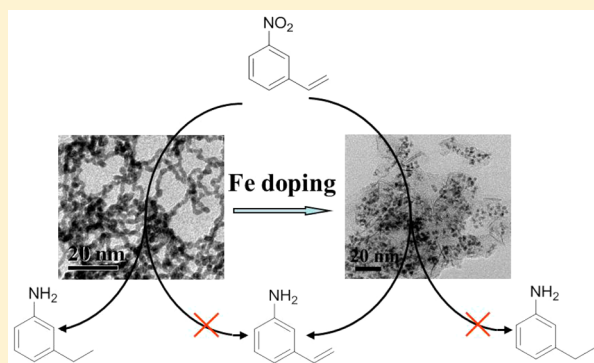


# Structure Evolution and Hydrogenation Performance of IrFe Bimetallic Nanomaterials

Ting Lu, Jian Lin, Xin Liu, Xiaodong Wang,\* and Tao Zhang

State Key Laboratory of Catalysis, Dalian Institute of Chemical Physics, Chinese Academy of Sciences, 457 Zhongshan Road, Dalian 116023, P.R. China

**ABSTRACT:** By a reverse microemulsion method, a series of IrFe bimetallic nanomaterials of variable morphologies and compositions is synthesized and characterized by  $^{57}\text{Fe}$  Mössbauer spectroscopy, XRD, XPS, and TEM. The structure evolution, such as IrFe alloy nanoparticles to Ir nanoparticles on  $\text{Fe}_2\text{O}_3$  flakes, can be simply tuned by changing the molar ratio of Ir to Fe precursors. In terms of Fe, the relative content of IrFe alloy decreased with the increase of Fe species doped, while that of  $\text{Fe}_2\text{O}_3$  flakes increased until reached 100%. The as-prepared IrFe bimetallic nanomaterials were served as catalysts for the selective hydrogenation of 3-nitrostyrene to 3-aminostyrene, and it is found that the catalytic performance was related to the morphology and composition of these nanomaterials.  $\text{Ir}_1\text{Fe}_4$  was subsequently identified to be a highly active and exceedingly selective catalyst with good stability and recyclability for the hydrogenation of 3-nitrostyrene, underscoring a remarkable “synergistic effect” of the two metals appearing as the form of Ir nanoparticles loaded on  $\text{Fe}_2\text{O}_3$  flakes. For Ir nanoparticles, they act as an active species for the hydrogenation; for  $\text{Fe}_2\text{O}_3$  flakes, they favor the preferential adsorption of nitro groups, which account for the better chemoselectivity to objective product.



## INTRODUCTION

Inorganic nanostructures, which have at least one dimension between 1 and 100 nm by definition, have attracted immense interest in their syntheses, owing to their fascinating properties in both fundamental research and practical application.<sup>1–3</sup> Nanoparticles in their nanoscale dimensions exhibit unique electronic, spectroscopic and chemical properties due to their small size and high surface-to-volume ratio.<sup>4,5</sup> The chemical and physical properties so much as their functionality of the nanomaterials are strongly dependent on the size, shape, and architecture of the nanostructures.<sup>6,7</sup> Moreover, compared with single metal, bimetallic nanomaterials, which can be a random alloy, a core–shell structure, or just mixed monometallic nanoparticles, usually exhibit performance superior to their monometallic counterparts, which therefore have attracted a great deal of attention from both academic and industrial fields.<sup>8–10</sup>

Recently, nanoscale metal particles have been widely used as effective catalysts because of their high density of active sites.<sup>11,12</sup> Among different noble metals, iridium nanoparticles were found outstanding candidates owing to their high catalytic activity, stability and selectivity in many catalysis reactions like alkene hydrogenation,<sup>13</sup> CO oxidation,<sup>14</sup> oxygen reduction reaction,<sup>15</sup> and for direct methanol fuel cell reaction.<sup>16</sup> However, compared with other noble metals, the synthesis of size and shape controlled Ir nanostructures remains a challenge; there were only a few reports on the shape control of Ir nanomaterials, and most of them limited to nanopar-

ticles.<sup>12,17,18</sup> In our previous work, we have successfully synthesized Ir nanowires and studied their excellent catalytic performance on the selective hydrogenation of *o*-chloronitrobenzene.<sup>19</sup> Functionalized anilines are important intermediates for the manufacture of many agrochemicals, pharmaceuticals, dyes and pigments.<sup>20–23</sup> Although the hydrogenation of simple aromatic nitroarenes to corresponding aniline derivatives poses few problems and is carried out catalytically on very large scales, it is still difficult to catalytically reduce the nitro group in a selective manner or needs harsh reaction conditions when the reactant contains other reducible functional groups (e.g., C=C, C≡C, C=O, C≡N, etc.). The good chemoselective hydrogenation of Ir nanowires on *o*-chloronitrobenzene has inspired us to explore Ir nanowires in the hydrogenation of nitroarenes with other reducible functional groups. However, it was found that both  $-\text{NO}_2$  and  $-\text{C}\equiv\text{C}$  groups were reduced in the hydrogenation of 3-nitrostyrene over Ir nanowires, suggesting that Ir nanowires exhibit no chemoselectivity to 3-aminostyrene. However, as mentioned above, Ir-based catalysts were usually used in many catalysis reactions, consequently showing high expectations to utilize the Ir nanowires in the selective hydrogenation of nitroarenes. Thus, how to realize the chemoselective hydrogenation of the nitro group to the desired 3-aminostyrene with the preservation

**Received:** December 14, 2015

**Revised:** March 2, 2016

of C=C double bond, especially under mild reaction conditions is now the problem we faced.

To solve this problem, many strategies are commonly desirable, based on the catalyst itself or introducing another component. It has been demonstrated that the selectivity of hydrogenation by monometallic nanoparticles can be improved by doping a selected metal.<sup>24,25</sup> Among these methods, bimetallic nanoparticles, which are widely applicable to heterogeneous transformations, frequently exhibit catalytic performance superior to their monometallic counterparts, a phenomenon referred as “synergistic effect”.<sup>9,26</sup> For example, Pd–Ag bimetallic systems are widely used as selective hydrogenation catalysts,<sup>27</sup> Fe-doping Rh/Fe nanoparticle catalyst shows dramatically enhanced catalytic performance for nitroarene hydrogenation,<sup>28</sup> and Ir–Fe system is more amenable than either Pt–Fe or Pd–Fe as redox sensors for use in hydrothermal experiments.<sup>29</sup> Thus, it is expected that the introduction of another metal into Ir precursor can improve the performance in selective hydrogenation reaction.

In this Article, we have facilely synthesized a series of IrFe bimetallic nanomaterials by reverse microemulsion technique and studied the effects of Fe doping on the structure evolution and catalytic performance of Ir precursor. According to the chemical valence of Fe and the morphology of the materials, the bimetallic nanostructures can be classified as single IrFe alloy nanoparticles, IrFe alloy nanoparticles coexisting with Fe<sub>2</sub>O<sub>3</sub> flakes, or Ir nanoparticles loaded on Fe<sub>2</sub>O<sub>3</sub> flakes. These bimetallic nanomaterials are explored as highly active and selective catalysts in the hydrogenation of 3-nitrostyrene under mild conditions.

## EXPERIMENTAL SECTION

**Catalyst Preparation.** Microemulsion was first fabricated by CTAB/water/*n*-heptane/*n*-hexanol with CTAB (cetyltrimethylammonium bromide, purchased from SIGMA-Aldrich Co. with purity  $\geq 99\%$ ) weight of 2.0 g (0.17 mol/L), *n*-heptane volume of 20 mL, and *n*-hexanol volume of 12 mL, which was equilibrated at 60 °C. Then, aqueous solutions of H<sub>2</sub>IrCl<sub>6</sub> (0.5 mol/L) and FeCl<sub>3</sub> (0.5 mol/L) at various desired molar ratios and total 1 mL volume were respectively added with continual stirring. The solution turned into dark brown color, which was still heated at 60 °C and stirred at least for 2 h. After that, 1.5 mL of freshly prepared 2 mol/L NaBH<sub>4</sub> aqueous solution was added dropwise under vigorous stirring. The color of the solution quickly turned from dark brown to black. Finally, the resultant mixture was incubated for 2 h with continuous stirring before being repeatedly washed with ethanol and water at least three times, respectively. The crude product was then retrieved by centrifugation and dried in a vacuum at 80 °C for 8 h. The used Fe<sub>2</sub>O<sub>3</sub> and Ir nanoparticles in Table 2 were purchased from Aladdin Chemistry Co. Ltd. with 99.5% purity and prepared according to the published paper,<sup>19</sup> respectively.

**Catalyst Characterization.** X-ray diffraction (XRD) patterns were collected on a PANalytical X'pert diffractometer equipped with Cu K $\alpha$  radiation ( $\lambda = 1.54184 \text{ \AA}$ ), operated at 40 kV and 40 mA. The morphologies of the samples were observed with transmission electron microscopy (TEM) using a JEM-2100F (JEOL) electronic microscope with an accelerating voltage of 200 kV. Before TEM experiments, the samples were ultrasonically dispersed in ethanol and then a drop of the solution was put onto a copper grid coated with a thin holey carbon film. The binding energies of surface species were determined by X-ray photoelectron spectra (XPS) on an ESCALAB250 X-ray photoelectron spectrometer with contaminated C as internal standard (C 1s = 284.5 eV) and special agglutinant containing the elements C, O and Si, was used to fix the sample and sampler. <sup>57</sup>Fe Mössbauer spectra were recorded using a Topologic 500A spectrometer and a proportional counter at room temperature. <sup>57</sup>Co(Rh) moving in a constant acceleration mode was used as radioactive source.

Accordingly, <sup>57</sup>Fe Mössbauer spectral parameters such as the isomer shift (IS), the electric quadrupole splitting (QS), the full line width at half-maximum (fwhm), and the relative spectral area (*A*) of different components on the absorption patterns were calculated. The IS values were quoted relative to  $\alpha$ -Fe at room temperature.

**Catalytic Testing.** The hydrogenation of 3-nitrostyrene was conducted in an autoclave equipped with a pressure control system. In each reaction, a mixture of IrFe catalyst (10 mg), inert SiO<sub>2</sub> (90 mg, which was used just to eliminate the effect of reactant diffusion due to the small amount of catalyst), reactant 3-nitrostyrene (0.5 mmol), internal standard *o*-xylene (0.25 mmol) and solvent toluene, in a total volume of 5 mL was placed into the autoclave. When the autoclave was sealed, air was purged by flushing with high pressure hydrogen more than 10 times. Then, the initial H<sub>2</sub> pressure was adjusted to 3 bar and the autoclave was equilibrated in a thermostatic bath at 40 °C. A magnetic stirring of 1200 r/min which is large enough to eliminate the external diffusion effect was carried out to initiate the reaction when the temperature of the thermocouple inserted was up to 40 °C. The H<sub>2</sub> pressure decreased gradually during the reaction as a result of hydrogenation. The reaction time was determined after many times experiments to the maximum of the conversion. After reaction, the product was analyzed by GC.

## RESULTS AND DISCUSSION

**Nanomaterials Characterization.** <sup>57</sup>Fe Mössbauer spectroscopy was employed to characterize the chemical state of iron in IrFe bimetallic nanomaterials. As seen from Figure 1

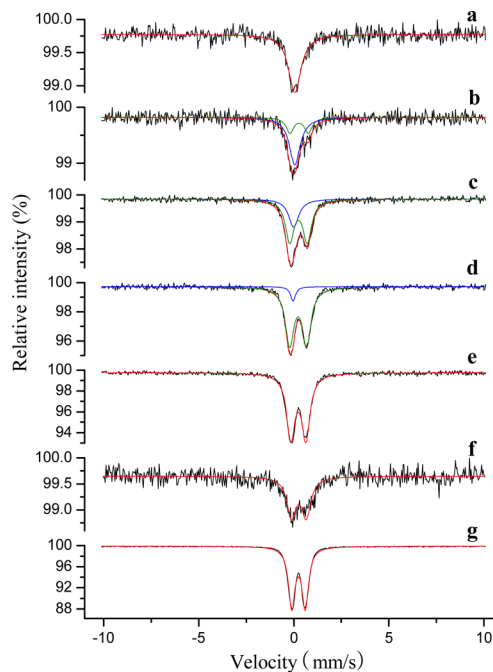


**Figure 1.** Room temperature <sup>57</sup>Fe Mössbauer spectra for IrFe nanomaterials at various Ir/Fe molar ratios: (a) 4/1, (b) 2/1, (c) 1/1, (d) 1/2, (e) 1/4, (f) spent 1/4, and (g) 0/1.

and Table 1, when Ir to Fe molar ratio was 4/1, a singlet peak was observed with IS value of 0.05, which is very close to that of Fe<sup>0</sup>. Combined with the XPS binding energy of Ir 4f<sub>7/2</sub> (60.7 eV, Figure 2b derived from Figure 2a), which corresponds to Ir<sup>0</sup>, it is indicated that Fe species was present as IrFe alloy without any protection (following XRD result further confirmed this view). It should be mentioned that although the XPS peak of Fe 2p<sub>3/2</sub> at 711 eV (Figure 2c) corresponding to Fe<sup>3+</sup> was examined for Ir/Fe = 4/1 sample, it was very weak and almost could be ignored. It may be attributed to the

**Table 1. Room Temperature  $^{57}\text{Fe}$  Mössbauer Parameters of IrFe Nanomaterials at Various Ir/Fe Molar Ratios**

entry	Ir/Fe (mol/mol)	subspectra	oxidation state of iron	IS (mm/s) <sup>a</sup>	QS (mm/s) <sup>b</sup>	spectral area (%) <sup>c</sup>	fwhm (mm/s)
1	4/1	singlet	$\text{Fe}^0$	0.05	0	100	0.79
2	2/1	singlet	$\text{Fe}^0$	0.05	0	69.3	0.69
		doublet	$\text{Fe}^{3+}$	0.28	0.97	30.7	0.48
3	1/1	singlet	$\text{Fe}^0$	-0.01	0	28.7	0.65
		doublet	$\text{Fe}^{3+}$	0.25	0.93	71.3	0.55
4	1/2	singlet	$\text{Fe}^0$	-0.04	0	6.9	0.31
		doublet	$\text{Fe}^{3+}$	0.23	0.89	93.1	0.54
5	1/4	doublet	$\text{Fe}^{3+}$	0.24	0.79	100	0.53
6 <sup>d</sup>	1/4 (spent)	doublet	$\text{Fe}^{3+}$	0.27	0.77	100	0.58
7	0/1	doublet	$\text{Fe}^{3+}$	0.24	0.71	100	0.42

<sup>a</sup> $\delta$ , isomer shift, related to  $\alpha\text{-Fe}$ . <sup>b</sup>QS, electric quadrupole splitting. <sup>c</sup>Uncertainty is  $\pm 5\%$  of reported value. <sup>d</sup>Entry 6 lists the room temperature  $^{57}\text{Fe}$  Mössbauer parameters of spent  $\text{Ir}_1\text{Fe}_4$  nanomaterial after five cycles of 3-nitrostyrene hydrogenation.

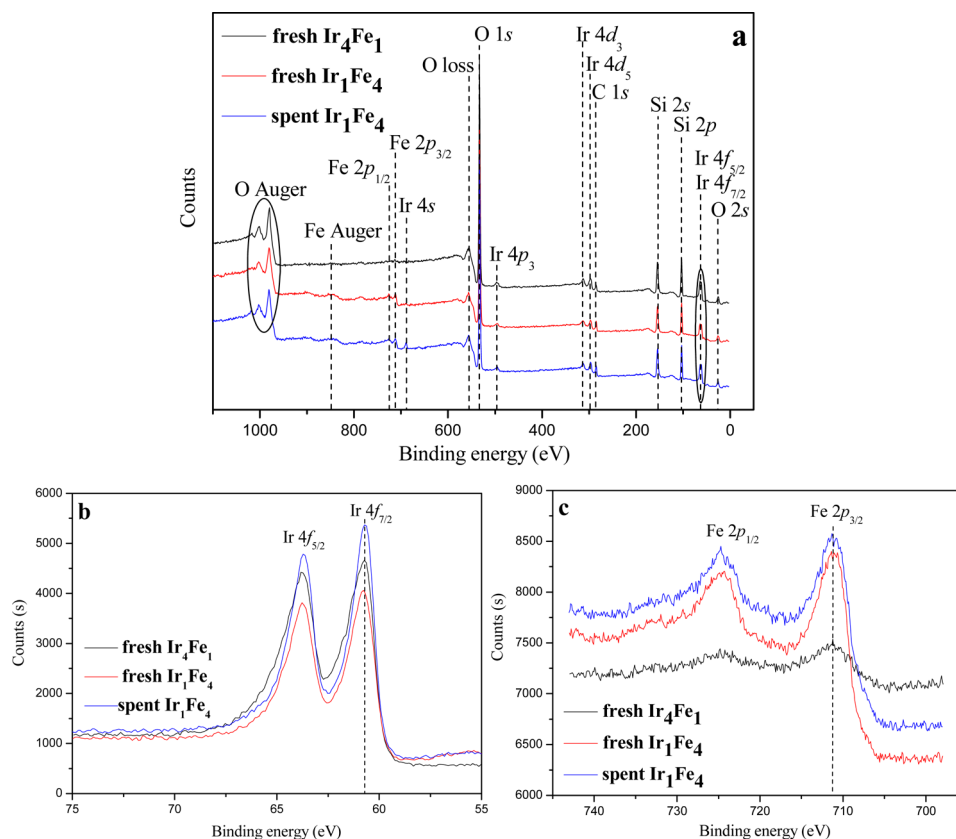


**Figure 2.** XPS spectra for IrFe nanomaterials at Ir/Fe molar ratios of 4/1 and 1/4 before and after five cycles hydrogenation: (a) surveys; (b) Ir windows; (c) Fe windows.

oxidation of little Fe exposed on the sample surface which was not alloy with Ir. Because the amount of this oxidized  $\text{Fe}^{3+}$  was very few, it is less than the error range and cannot be examined by Mössbauer spectroscopy preferring to the bulk property. When Ir/Fe = 2/1, besides the IrFe alloy singlet peak, a new doublet subspectrum corresponding to  $\text{Fe}^{3+}$  ( $\text{Fe}_2\text{O}_3$ ) appeared, and the relative spectral area was 30.7%. Further increasing Fe content from Ir/Fe = 1/1 to 1/2, the relative content of IrFe alloy decreased from 28.7% to 6.9%, while that of  $\text{Fe}^{3+}$  increased from 71.3% to 93.1%. Particularly, when Ir/Fe reached 1/4, the state of Fe species in IrFe bimetallic nanomaterials was approximate to that of sole  $\text{Fe}^{3+}$  sample (Ir/Fe = 0/1), suggesting that IrFe alloy absolutely disappeared and Fe species existed as 100%  $\text{Fe}^{3+}$ . Meanwhile, for Ir species, XPS results (Figure 2b) revealed it still existed as a form of  $\text{Ir}^0$

at Ir/Fe = 1/4 and Fe species existed as a form of  $\text{Fe}^{3+}$  (Figure 2c). Combined with Mössbauer measurement results, it can be concluded that, with the doping of Fe species into Ir precursor, not only the chemical states of Ir and Fe species but also the relative proportions of different Fe species are modulated. Specifically, with the increase of Fe content in IrFe bimetallic nanomaterials, the Ir and Fe species changed from 100% IrFe alloy to the coexistence of IrFe alloy and  $\text{Fe}_2\text{O}_3$ , and finally to single metal Ir coexisting with  $\text{Fe}_2\text{O}_3$ . Detailed morphologies are characterized in the following text.

Figure 3 shows the XRD patterns of IrFe bimetallic nanomaterials at various Ir/Fe molar ratios. In the case of the sole Fe sample (Figure 3a(8)), the major diffraction peaks with  $2\theta$  values of  $35.6^\circ$  and  $62.8^\circ$  can be indexed to the (311) plane and (440) plane of maghemite  $\text{Fe}_2\text{O}_3$  (PDF #00-024-0081).

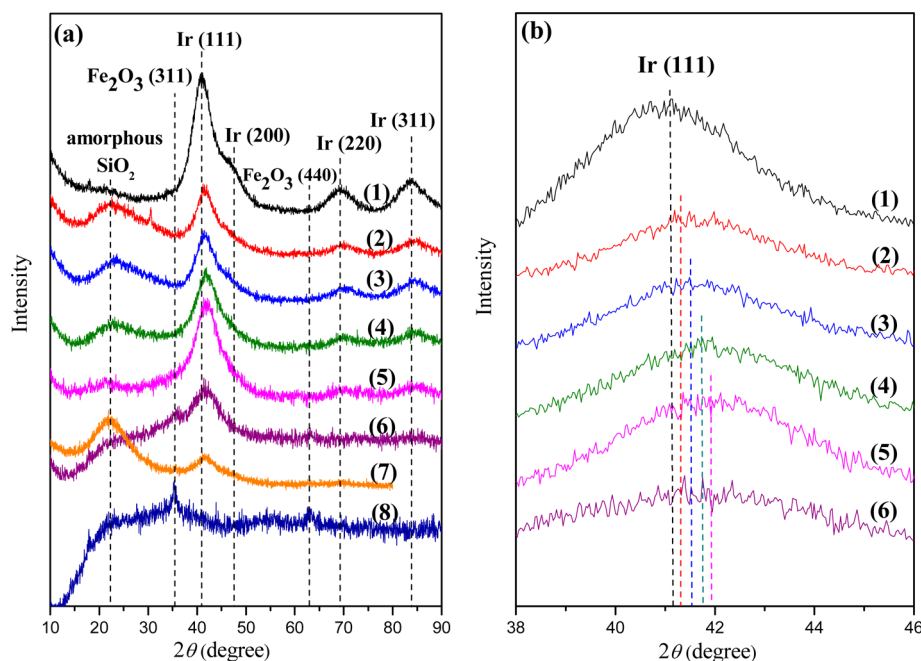


**Figure 3.** Whole (a) and local magnified (b) XRD patterns for IrFe nanomaterials at various Ir/Fe molar ratios: (1) 1/0, (2) 4/1, (3) 2/1, (4) 1/1, (5) 1/2, (6) 1/4, (7) spent 1/4, and (8) 0/1.

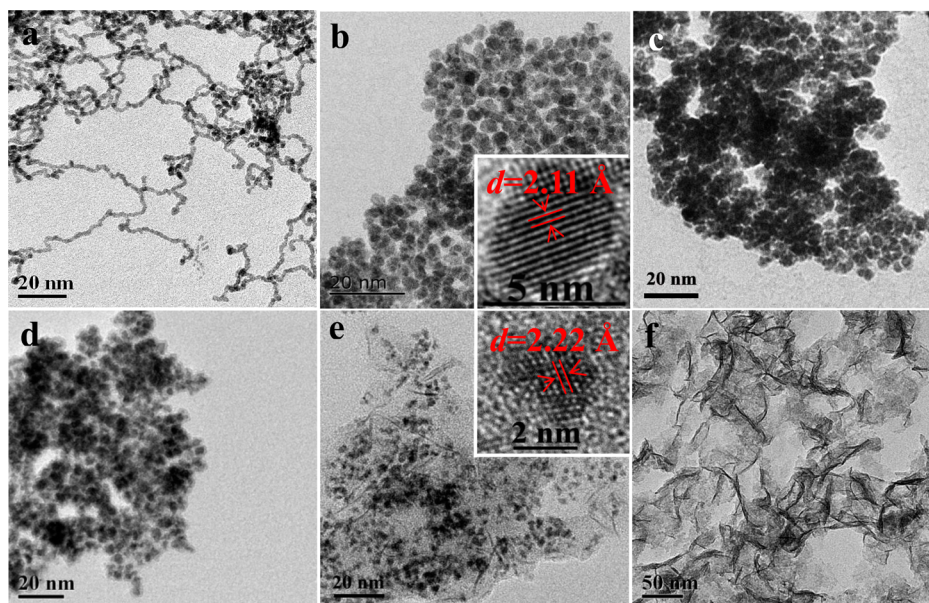


**Figure 4.** TEM and HRTEM images for IrFe nanomaterials at various Ir/Fe molar ratios: (a) 1/0, (b) 4/1, (c) 2/1, (d) 1/2, (e) 1/4, and (f) 0/1.

For all the IrFe bimetallic nanomaterials with different Ir-to-Fe ratios, two main diffraction peaks were still related to sole Ir sample (Figure 3a(1), PDF #00-006-0598). Moreover, a diffraction peak at about  $22.2^\circ$  assigned to the amorphous  $\text{SiO}_2$  was present for all the samples with different intensities, which was induced by the sample platform containing  $\text{SiO}_2$ .<sup>30</sup> It is also found that with the increase of Fe content, the noise of baselines increased, which probably induced by the increase of amorphous part linked to  $\text{Fe}_2\text{O}_3$ . Notably, as the content of Fe increased from Ir/Fe = 4/1 to Ir/Fe = 1/2, the peaks for Ir(111) (original  $41.1^\circ$ , Figure 3b(1)) shifted to  $41.3^\circ$ ,  $41.5^\circ$ ,  $41.7^\circ$ , and  $41.9^\circ$ , respectively (Figure 3b(2)–(5)). This shift in  $2\theta$  values could be attributed to the formation of IrFe alloy, which is in good agreement with the Mössbauer results.

Interestingly, when Ir/Fe = 1/4 (Figure 3a(6)), no obvious peak shift can be observed, indicating that IrFe alloy was nearly no longer formed. Instead, two small  $\text{Fe}_2\text{O}_3$  peaks (311) and (400) besides the characteristic Ir(111) were detected, in accordance with the Mössbauer result that only  $\text{Fe}^{3+}$  without IrFe alloy existed at Ir/Fe = 1/4.

TEM characterization was performed and representative images are shown in Figure 4. For pure Ir, one-dimensional Ir nanowires with 2 nm diameter were obtained (Figure 4a). When doping a little amount of Fe species into Ir precursor, nanoparticles but not nanowires were observed at Ir/Fe = 4/1 (Figure 4b), which possessed 5 nm size. The formation of nanoparticles may be attributed to the specific interactions among IrFe nanocrystals and surfactant molecules arising from

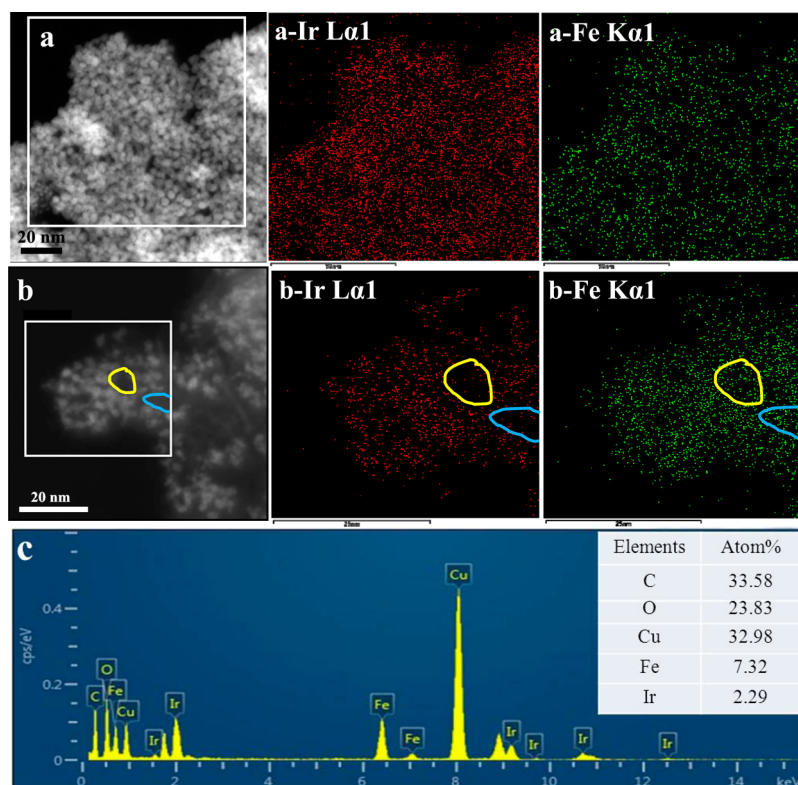


**Figure 5.** STEM and EDS mapping images and bulk elemental analysis for IrFe nanomaterials at Ir/Fe molar ratios of 4/1 (a) and 1/4 (b,c).

Fe species doping, which restricts the growth of surfactant-encapsulated primary nanoparticles into nanowires. Combined with the Mössbauer and XRD results (Figures 1a and 3a(2)), these nanoparticles were IrFe alloy nanoparticles. HRTEM image in the inset of Figure 4b particularly verified the formation of IrFe alloy that the observed plane spacing of 2.11 Å deviated from the major component Ir of the most obvious crystal facets (111) (2.20 Å). Element Ir and Fe EDS mappings for Ir/Fe = 4/1 (Figure 5a) also showed the uniformity and synchronicity of Ir and Fe distribution. Further increasing the doping amount of Fe species to Ir/Fe = 2/1 (Figure 4c), besides nanoparticles, some thin flakes were dimly visible. With the increase of Ir/Fe = 1/2, the flakes looked more clearly on which still loaded some nanoparticles (Figure 4d). Based on the Mössbauer measurement results, molar Fe species distributed as 69.3% Fe<sup>0</sup> and 30.7% Fe<sup>3+</sup> at Ir/Fe = 2/1, and 6.9% Fe<sup>0</sup> and 93.1% Fe<sup>3+</sup> at Ir/Fe = 1/2. Thus, it can be concluded that the nanoparticles corresponded to 5 nm IrFe alloy nanoparticles and the flakes corresponded to thin Fe<sub>2</sub>O<sub>3</sub> flakes at Ir/Fe = 2/1 and 1/2. Further increasing Ir/Fe = 1/4, the flakes still can be observed clearly, on which 2 nm smaller nanoparticles other than 5 nm IrFe alloy nanoparticles were loaded (Figure 4e). According to Mössbauer and XPS results, the Fe species was totally Fe<sub>2</sub>O<sub>3</sub> and the Ir species was single metal Ir at Ir/Fe = 1/4, thus it can be deduced that Fe species presented as Fe<sub>2</sub>O<sub>3</sub> flakes and Ir species existed as nanoparticles with size of 2 nm supported on Fe<sub>2</sub>O<sub>3</sub> flakes. Meanwhile, the statistical plane spacing of 2.22 Å (inset in Figure 4e) just corresponded to Ir(111). Compared with EDS mapping of element Ir (Figure 5b), that of element Fe looked uniform without any obvious gap in the regions marked by yellow and blue circles where there were nearly no Ir nanoparticles observed according to STEM image; while for element Ir, there were a few

distribution dots. It can be attributed to that at Ir/Fe = 1/4, Fe species formed continuous Fe<sub>2</sub>O<sub>3</sub> flakes while Ir species presented as 2 nm nanoparticles distributed on Fe<sub>2</sub>O<sub>3</sub> flakes randomly. Moreover, the selected-area bulk elemental analysis (Figure 5c) showed no other peaks except for C, O, Ir, Fe and Cu (derived from copper grid) can be detected, indicating the disposal of reduced agent and surfactant. And the bulk composition of Ir/Fe was close to 1/3.2, which deviated only a little from the designed composition of Ir/Fe = 1/4. When the doping amount of Fe species reached the ultimate value, that is, Ir/Fe = 0/1, thin flakes with obvious crinkles were obtained by TEM observation (Figure 4f). That is to say, for pure Fe species, it existed as thin Fe<sub>2</sub>O<sub>3</sub> flakes totally by our reverse microemulsion method.

According to the above results, it could be concluded that doping of Fe species into Ir precursor can change and modulate the existing form, morphology and distribution of both Ir and Fe species. From the viewpoint of H<sub>2</sub>IrCl<sub>6</sub> microemulsion, the addition of Fe<sup>3+</sup> not only increases the ionic strength of the solution, but also compresses the double layer around the polar headgroups and screens the electrostatic repulsion between the charged headgroups of CTAB. Thus, the area per headgroup of the surfactant molecule is decreased, resulting in the increase of the critical packing parameter  $p^{31-33}$  which is beneficial to the formation of larger assemblies such as reverse micelles ( $p$  is defined as  $v/a_0l_c$ , where  $v$  is the hydrophobic portion of the surfactant,  $a_0$  is the equilibrium area per molecule at the aggregate surface, and  $l_c$  is the length of the hydrophobic group;  $0 \leq p \leq 1/3$  for spherical micelles,  $1/3 \leq p \leq 1/2$  for cylindrical micelles,  $1/2 \leq p \leq 1$  for bilayer structures, and  $p > 1$  for inverted micelles). Moreover, the addition of Fe<sup>3+</sup> would influence the specific interactions among IrFe nanocrystals, surfactant molecules and excess NaBH<sub>4</sub>, preventing the

Table 2. Hydrogenation of 3-Nitrostyrene over IrFe Nanomaterials at Various Ir/Fe Molar Ratios<sup>a</sup>

entry	Ir/Fe (mol/mol)	morphology	reaction time (min)	conversion (%)	selectivity to 2a (%)	TON <sup>f</sup>
1	1/0	Ir NWs <sup>b</sup>	15	98	2	9.4
2	4/1	IrFe NPs <sup>c</sup>	24	95	3	9.8
3	2/1	IrFe NPs on Fe <sub>2</sub> O <sub>3</sub> flakes	19	91	71	10.0
4	1/1	IrFe NPs on Fe <sub>2</sub> O <sub>3</sub> flakes	135	83	90	10.3
5	1/2	IrFe NPs on Fe <sub>2</sub> O <sub>3</sub> flakes	195	86	96	13.1
6	1/4	Ir NPs on Fe <sub>2</sub> O <sub>3</sub> flakes	105	93	92	19.3
7	0/1	Fe <sub>2</sub> O <sub>3</sub> flakes	420	0	0	0
8	0/1	Fe <sub>2</sub> O <sub>3</sub> NPs <sup>d</sup>	240	0	0	0
9	1/4	Ir NPs <sup>e</sup> + Fe <sub>2</sub> O <sub>3</sub> flakes	12	99	0	25.4

<sup>a</sup>Reaction conditions:  $T = 40\text{ }^{\circ}\text{C}$ ,  $p = 3\text{ bar}$ ; 10 mg of catalyst + 90 mg of SiO<sub>2</sub>, 0.5 mmol 3-nitrostyrene, 5 mL of toluene solvent, *o*-xylene as internal standard. <sup>b</sup>NWs: nanowires. <sup>c</sup>NPs: nanoparticles. <sup>d</sup>Fe<sub>2</sub>O<sub>3</sub> nanoparticles were purchased from Aladdin Chemistry Co. Ltd. with 99.5% purity and 10 nm size. <sup>e</sup>Ir nanoparticles were prepared according to the published paper<sup>19</sup> with 2 nm size. <sup>f</sup>TON (turnover number), specific activity per Ir atom for 3-nitrostyrene hydrogenation at the maximum conversion.

aggregation of surfactant-encapsulated primary nanoparticles into nanowires. On the other hand, as an important synthesis parameter, the Ir/Fe/NaBH<sub>4</sub> ratio, plays a key role in regulating the composition and morphology of the final IrFe bimetallic products. As a versatile reducing agent, NaBH<sub>4</sub> is frequently used in a wide range of reduction process.<sup>34</sup> In our synthesized process, fixed and excess NaBH<sub>4</sub> with 6 times molar ratios of NaBH<sub>4</sub> to H<sub>2</sub>IrCl<sub>6</sub> and FeCl<sub>3</sub> was used to ensure the complete reduction of Ir and Fe species. With the variation of H<sub>2</sub>IrCl<sub>6</sub> to FeCl<sub>3</sub> molar ratios, the morphology of IrFe nanomaterials changed from entire 5 nm IrFe alloy nanoparticles to the coexistence of 5 nm IrFe alloy nanoparticles and Fe<sub>2</sub>O<sub>3</sub> flakes, and finally to 2 nm Ir nanoparticles loaded on Fe<sub>2</sub>O<sub>3</sub> flakes. Based on Vegard's law:<sup>35</sup>

$$d_0^{\text{Ir}_x\text{Fe}_{1-x}} = x d_0^{\text{Ir}} + (1 - x) d_0^{\text{Fe}}$$

We made a calculation of the qualitative phase composition of IrFe alloy in different Ir/Fe ratios using the peak with the highest intensity in XRD (Figure 3b), where  $d_0$  are the lattice constants for IrFe alloy, Ir, and Fe, which were calculated through MDI Jade5.0 software, and  $x$  is the molar fraction of Ir in IrFe alloy. The alloys were Ir<sub>94</sub>Fe<sub>6</sub> for Ir/Fe = 4/1 and 2/1, Ir<sub>92</sub>Fe<sub>8</sub> for Ir/Fe = 1/1, and Ir<sub>90</sub>Fe<sub>10</sub> for Ir/Fe = 1/2. Clearly, the phase composition of IrFe alloy contained at least 90% Ir and the molar fraction of Fe less than 10%. That is to say, when the relative amount of Fe species was small, a limited content of Fe species enter the crystal lattice of Ir after the addition of NaBH<sub>4</sub> and satisfied the requirement of crystal lattice matching to form IrFe alloy. When the relative content of Fe species was large, the excessive Fe species no longer satisfied the crystal lattice matching of IrFe alloy formation, thus the phase separation of Ir and Fe species occurred, resulting in the formation of Ir nanoparticles and Fe<sub>2</sub>O<sub>3</sub> flakes, respectively.

**Catalytic Activity.** The catalytic performance of IrFe nanomaterials was evaluated in the selective hydrogenation of 3-nitrostyrene under mild reaction conditions (3 bar, 40 °C), as shown in Table 2. As the benchmark, pure Ir nanowires showed good activity but very low selectivity to the desired product 2a<sup>36</sup> (entry 1); nearly all the -NO<sub>2</sub> and -C=C were reduced. With the addition of Fe, the catalytic performance of Ir<sub>4</sub>Fe<sub>1</sub> was found to be same as that of pure Ir nanowires (entry 2). Interestingly, a considerable improvement in the selectivity was

observed with further increasing amount of Fe species (entries 3–6), that is, a good chemoselectivity toward the reduction of nitro group, and afforded the desired 3-aminostyrene product without the reduction of C=C to 3-ethylaniline. The best result was obtained with Ir<sub>1</sub>Fe<sub>4</sub> (entry 6), over which both conversion and selectivity achieved more than 90%. This performance was comparable to those over Pt- and Fe<sub>2</sub>O<sub>3</sub>-based catalysts.<sup>22,36</sup> Moreover, the whole amount of Ir component was used to calculate TON only for reference. As shown, the TON values increased with the increasing content of Fe in IrFe bimetallic nanomaterials, and the maximum value of TON was observed over the mixture of Ir nanoparticles and Fe<sub>2</sub>O<sub>3</sub> flakes.

The kinetic studies were carried out to follow the variations of conversion, yield and pressure versus time. Here, the yield was defined as reactant conversion × product selectivity to 3-aminostyrene listed in Table 2. As shown in Figure 6, the pressure decreased gradually with the reaction time, and the conversion and yield first increased quickly then became gently and finally decreased after 105 min reaction over Ir<sub>1</sub>Fe<sub>4</sub>. Control test over either Fe<sub>2</sub>O<sub>3</sub> flakes or Fe<sub>2</sub>O<sub>3</sub> nanoparticles (entries 7 and 8 in Table 2) under identical reaction conditions

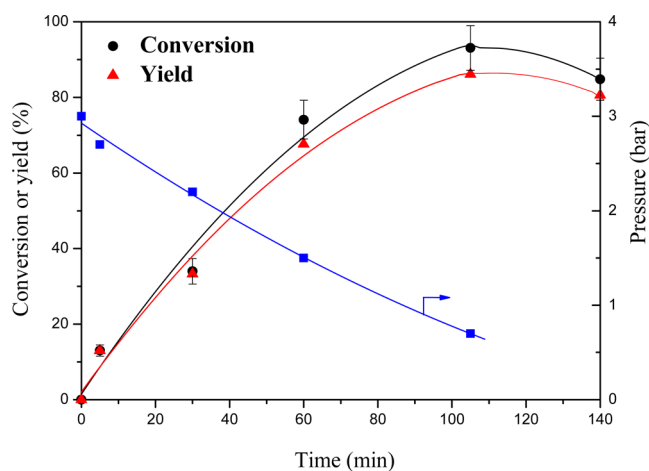


Figure 6. Kinetic curves for 3-nitrostyrene hydrogenation with Ir<sub>1</sub>Fe<sub>4</sub> under 40 °C and 3 bar.

did not show any activity at all, highlighting the critical role of Ir component.

The above-mentioned results demonstrated that on the basis of keeping high conversion, the introduction of Fe species into Ir precursor dramatically changes the chemoselectivity to the objective product 3-aminostyrene. Combined the catalytic activity with Mössbauer characterization (entry 1 in Table 1), it can be found that without  $\text{Fe}_2\text{O}_3$  flakes formation, the selectivity to objective product 2a was very low (entry 2 in Table 2), indicating that the IrFe alloy nanoparticles hardly make a contribution to the selectivity. With further increase of Fe content, the relative content of IrFe alloy decreased and that of  $\text{Fe}_2\text{O}_3$  flakes increased; correspondingly, the selectivity to objective product 2a increased. Clearly, the formation of  $\text{Fe}_2\text{O}_3$  flakes makes a positive contribution to the selectivity. However, this result did not mean that the contribution of Ir can be ignored; instead, it plays an important role in the reaction. Taking  $\text{Ir}_1\text{Fe}_4$  for an example, the participation of Fe species dramatically improved the selectivity of Ir nanowires from 2% to 92%. It should be emphasized that the Ir nanoparticles and  $\text{Fe}_2\text{O}_3$  flakes did not separate from each other, but “synergistic effect” existed between them. Physically mixing Ir nanoparticles (2 nm, synthesized according to the previous paper<sup>39</sup>) with  $\text{Fe}_2\text{O}_3$  flakes with a molar ratio of 1/2 to simulate  $\text{Ir}_1\text{Fe}_4$  composite in the hydrogenation reaction, it is found that, similar to pure Ir nanowires or Ir nanoparticles, this mixture did not possess the chemoselectivity toward the reduction of nitro group and did not afford the desired 3-aminostyrene product at all (entry 9 in Table 2). The absolutely different chemoselectivity between  $\text{Ir}_1\text{Fe}_4$  and mixture of Ir nanoparticles and  $\text{Fe}_2\text{O}_3$  flakes proved that the Ir nanoparticles and  $\text{Fe}_2\text{O}_3$  flakes are not absolutely dissociative but there is indeed some synergistic effect affecting the nature of chemoselectivity. It is also found from the XPS result (Figure 2b) that compared with  $\text{Ir}_4\text{Fe}_1$  (60.7 eV) no significant binding energy shift of Ir  $4f_{7/2}$  can be observed in  $\text{Ir}_1\text{Fe}_4$  (60.8 eV), indicating that the interaction between Ir and Fe species in  $\text{Ir}_1\text{Fe}_4$  was comparable to that in  $\text{Ir}_4\text{Fe}_1$  alloy.<sup>37</sup> In other words, similar to the strong interaction of Ir and Fe species in  $\text{Ir}_4\text{Fe}_1$  alloy, there was also a strong interaction between the components in  $\text{Ir}_1\text{Fe}_4$ . It is proposed that the chemoselective hydrogenation of nitro groups arises from the preferential and strong adsorption of nitro groups on the specific sites of  $\text{Fe}_2\text{O}_3$  flakes,<sup>38,39</sup> and the Ir nanoparticles played a major role in activating the hydrogen.<sup>23</sup> The  $\text{N}_2$  adsorption/desorption results (Figure 7) just proved the above viewpoint that the BET surface area of  $\text{Ir}_1\text{Fe}_4$  (Ir nanoparticles @  $\text{Fe}_2\text{O}_3$  flakes,  $82.6 \pm 0.4 \text{ m}^2/\text{g}$ ) was much larger than that of  $\text{Ir}_4\text{Fe}_1$  (IrFe alloy nanoparticles,  $8.1 \pm 0.04 \text{ m}^2/\text{g}$ ), which is consistent with their catalytic performance in traditional understand. Meanwhile, it indicated that the formation of  $\text{Fe}_2\text{O}_3$  flakes was beneficial to the increase of surface area compared with that of IrFe alloy nanoparticles.

The stability of IrFe bimetallic nanomaterials as a catalyst was also explored. Taking the best  $\text{Ir}_1\text{Fe}_4$  for an example, the IrFe nanomaterial could be easily recycled by centrifugation, without visible decay in activity and selectivity for at least five cycles (Figure 8). After the fifth cycle, ICP-MS result showed that there were no Ir and Fe species in the filtrate that can be observed to the detectable limits, indicating that leaching does not occur and the reaction is catalyzed exclusively by the heterogeneous  $\text{Ir}_1\text{Fe}_4$  composite, i.e. Ir nanoparticles loaded on  $\text{Fe}_2\text{O}_3$  flakes. Subsequently, the spent  $\text{Ir}_1\text{Fe}_4$  nanomaterial after five cycles hydrogenation was characterized by  $^{57}\text{Fe}$  Mössbauer

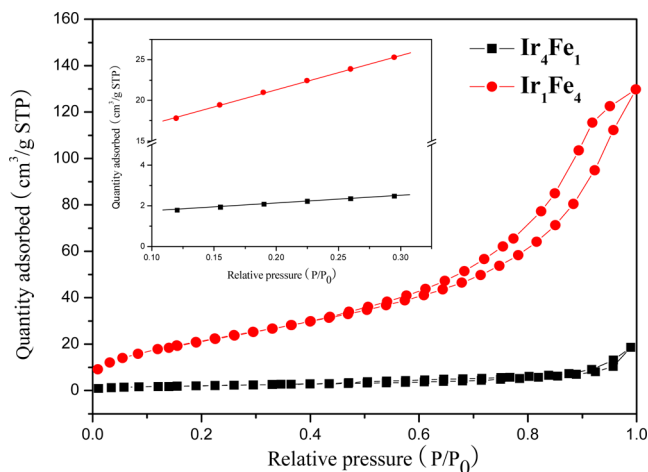


Figure 7.  $\text{N}_2$  adsorption/desorption isotherms of  $\text{Ir}_4\text{Fe}_1$  and  $\text{Ir}_1\text{Fe}_4$  nanomaterials.

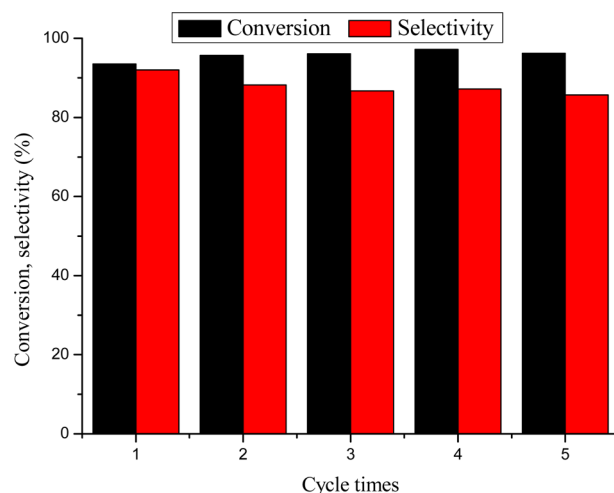


Figure 8. Cycle performance for  $\text{Ir}_1\text{Fe}_4$  nanomaterial.

spectroscopy, XPS, and XRD, as shown in Figures 1–3. It can be seen from Figure 1(f) that although the quality of Mössbauer spectrum looked poorer of spent  $\text{Ir}_1\text{Fe}_4$ , there was no obvious change on the Mössbauer parameters for the spent  $\text{Ir}_1\text{Fe}_4$  compared with those for the fresh one. From XPS spectra (Figure 2), the characteristic peak positions both for Ir and Fe windows hardly shifted before and after the reaction. For XRD pattern (Figure 3a(7)), there was also no obvious shift on amorphous  $\text{SiO}_2$  and Ir peak positions, only the relative intensities of them changed which was induced by the addition of  $\text{SiO}_2$  in the reaction. Combined with the good cycle performance, the above results confirmed the good stability of this nanomaterial.

## CONCLUSION

In summary, a series of IrFe bimetallic nanomaterials of variable morphologies and compositions is synthesized through doping Fe into Ir precursor by a reverse microemulsion method. The structure evolution of IrFe from entire 5 nm IrFe alloy nanoparticles to the coexistence of 5 nm IrFe alloy nanoparticles and  $\text{Fe}_2\text{O}_3$  flakes, and finally to 2 nm Ir nanoparticles loaded on  $\text{Fe}_2\text{O}_3$  flakes can be controlled by tuning the relative ratio of Ir-to-Fe precursors. The above IrFe nanomaterials with three kinds of microstructures are applied as catalysts in the

hydrogenation of 3-nitrostyrene to 3-aminostyrene under mild reaction conditions to evaluate their hydrogenation performance. It is found that the catalytic activity follows the sequence of Ir nanoparticles loaded on Fe<sub>2</sub>O<sub>3</sub> flakes > IrFe alloy nanoparticles coexisting with Fe<sub>2</sub>O<sub>3</sub> flakes ≫ IrFe alloy nanoparticles. The optimal catalyst with good stability and recyclability is obtained with Ir<sub>1</sub>Fe<sub>4</sub>, that is, 2 nm Ir nanoparticles loaded on Fe<sub>2</sub>O<sub>3</sub> flakes, over which both conversion and selectivity achieve more than 90%. Compared with monometallic Ir nanowires, Ir nanoparticles, or Fe<sub>2</sub>O<sub>3</sub> flakes, the excellent hydrogenation performance of Ir<sub>1</sub>Fe<sub>4</sub> emphasizes a remarkable “synergistic effect” between Ir nanoparticles and Fe<sub>2</sub>O<sub>3</sub> flakes. For Ir nanoparticles, they play the role of active centers to activate hydrogen; for Fe<sub>2</sub>O<sub>3</sub> flakes, they act as support and favor the preferential adsorption of nitro groups, which account for the high chemoselectivity. This work brings much interest in searching inexpensive metal doping bimetallic nanomaterials as selective catalysts for hydrogenation reaction.

## AUTHOR INFORMATION

### Corresponding Author

\*E-mail: [xdwang@dicp.ac.cn](mailto:xdwang@dicp.ac.cn). Tel: +86-411-84379680. Fax: +86-411-84685940.

### Notes

The authors declare no competing financial interest.

## ACKNOWLEDGMENTS

This work was supported by the National Natural Science Foundation of China (21003124, 21076211, 21203181, and 11205160).

## REFERENCES

- (1) Cushing, B. L.; Kolesnichenko, V. L.; O'Connor, C. J. Recent Advances in the Liquid-Phase Syntheses of Inorganic Nanoparticles. *Chem. Rev.* **2004**, *104*, 3893–3846.
- (2) Qi, L. M. Synthesis of Inorganic Nanostructures in Reverse Micelles. In *Encyclopedia of Surface and Colloid Science*, 2nd ed.; Somasundaran, P., Ed.; Chemical Rubber Company: New York, 2006, 6183–6207.
- (3) Cantillo, D.; Baghbanzadeh, M.; Kappe, C. O. In Situ Generated Iron Oxide Nanocrystals as Efficient and Selective Catalysts for the Reduction of Nitroarenes using a Continuous Flow Method. *Angew. Chem., Int. Ed.* **2012**, *51*, 10190–10193.
- (4) Shylesh, S.; Schünemann, V.; Thiel, W. R. Magnetically Separable Nanocatalysts: Bridges between Homogeneous and Heterogeneous Catalysis. *Angew. Chem., Int. Ed.* **2010**, *49*, 3428–3459.
- (5) Kwon, S. J.; Fan, F. R. F.; Bard, A. J. Observing Iridium Oxide (IrO<sub>x</sub>) Single Nanoparticle Collisions at Ultramicroelectrodes. *J. Am. Chem. Soc.* **2010**, *132*, 13165–13167.
- (6) Xie, X. W.; Li, Y.; Liu, Z. Q.; Haruta, M.; Shen, W. J. Low-Temperature Oxidation of CO Catalysed by Co<sub>3</sub>O<sub>4</sub> Nanorods. *Nature* **2009**, *458*, 746–749.
- (7) Juvé, V.; Cardinal, M. F.; Lombardi, A.; Crut, A.; Maioli, P.; Pérez-Juste, J.; Liz-Marzán, L. M.; Del Fatti, N.; Vallée, F. Size-Dependent Surface Plasmon Resonance Broadening in Nonspherical Nanoparticles: Single Gold Nanorods. *Nano Lett.* **2013**, *13*, 2234–2240.
- (8) Della Pina, C.; Falletta, E.; Rossi, M. Highly Selective Oxidation of Benzyl Alcohol to Benzaldehyde Catalyzed by Bimetallic Gold-Copper Catalyst. *J. Catal.* **2008**, *260*, 384–386.
- (9) Liu, X. Y.; Wang, A. Q.; Li, L.; Zhang, T.; Mou, C. Y.; Lee, J. F. Structural Changes of Au-Cu Bimetallic Catalysts in CO Oxidation: In situ XRD, EPR, XANES, and FT-IR Characterizations. *J. Catal.* **2011**, *278*, 288–296.
- (10) Cai, S. F.; Duan, H. H.; Rong, H. P.; Wang, D. S.; Li, L. S.; He, W.; Li, Y. D. Highly Active and Selective Catalysis of Bimetallic Rh<sub>3</sub>Ni<sub>1</sub> Nanoparticles in the Hydrogenation of Nitroarenes. *ACS Catal.* **2013**, *3*, 608–612.
- (11) Lewis, L. N. Chemical Catalysis by Colloids and Clusters. *Chem. Rev.* **1993**, *93*, 2693–2730.
- (12) Kundu, S.; Liang, H. Shape-Selective Formation and Characterization of Catalytically Active Iridium Nanoparticles. *J. Colloid Interface Sci.* **2011**, *354*, 597–606.
- (13) Dupont, J.; Fonseca, G. S.; Umpierre, A. P.; Fichtner, P. F. P.; Teixeira, S. R. Transition-Metal Nanoparticles in Imidazolium Ionic Liquids: Recyclable Catalysts for Biphasic Hydrogenation Reactions. *J. Am. Chem. Soc.* **2002**, *124*, 4228–4229.
- (14) Lin, J.; Qiao, B. T.; Liu, J. Y.; Huang, Y. Q.; Wang, A. Q.; Li, L.; Zhang, W. S.; Allard, L. F.; Wang, X. D.; Zhang, T. Design of a Highly Active Ir/Fe(OH)<sub>x</sub> Catalyst: Versatile Application of Pt-Group Metals for the Preferential Oxidation of Carbon Monoxide. *Angew. Chem., Int. Ed.* **2012**, *51*, 2920–2924.
- (15) Liu, G.; Zhang, H. Facile Synthesis of Carbon-Supported Ir<sub>x</sub>Se<sub>y</sub> Chalcogenide Nanoparticles and Their Electrocatalytic Activity for the Oxygen Reduction Reaction. *J. Phys. Chem. C* **2008**, *112*, 2058–2065.
- (16) Baglio, V.; Sebastian, D.; D'Urso, C.; Stassi, A.; Amin, R. S.; El-Khatib, K. M.; Arico, A. S. Composite Anode Electrode Based on Iridium Oxide Promoter for Direct Methanol Fuel Cells. *Electrochim. Acta* **2014**, *128*, 304–310.
- (17) Fonseca, G. S.; Umpierre, A. P.; Fichtner, P. F. P.; Teixeira, S. R.; Dupont, J. The Use of Imidazolium Ionic Liquids for the Formation and Stabilization of Ir<sup>0</sup> and Rh<sup>0</sup> Nanoparticles: Efficient Catalysts for the Hydrogenation of Arenes. *Chem. - Eur. J.* **2003**, *9*, 3263–3269.
- (18) Stowell, C. A.; Korgel, B. A. Iridium Nanocrystal Synthesis and Surface Coating-Dependent Catalytic Activity. *Nano Lett.* **2005**, *5*, 1203–1207.
- (19) Lu, T.; Wei, H. S.; Yang, X. F.; Li, J.; Wang, X. D.; Zhang, T. Microemulsion-Controlled Synthesis of One-Dimensional Ir Nanowires and Their Catalytic Activity in Selective Hydrogenation of *o*-Chloronitrobenzene. *Langmuir* **2015**, *31*, 90–95.
- (20) Blaser, H. U.; Siegrist, U.; Steiner, H. *Aromatic Nitro Compounds: Fine Chemicals through Heterogeneous Catalysis*; Wiley-VCH: Weinheim, 2001.
- (21) Corma, A.; Serna, P. Chemoselective Hydrogenation of Nitro Compounds with Supported Gold Catalysts. *Science* **2006**, *313*, 332–334.
- (22) Jagadeesh, R. V.; Surkus, A. E.; Junge, H.; Pohl, M. M.; Radnik, J.; Rabeah, J.; Huan, H. M.; Schünemann, V.; Brückner, A.; Beller, M. Nanoscale Fe<sub>2</sub>O<sub>3</sub>-Based Catalysts for Selective Hydrogenation of Nitroarenes to Anilines. *Science* **2013**, *342*, 1073–1076.
- (23) Wei, H. S.; Liu, X. Y.; Wang, A. Q.; Zhang, L. L.; Qiao, B. T.; Yang, X. F.; Huang, Y. Q.; Miao, S.; Liu, J. Y.; Zhang, T. FeO<sub>x</sub>-Supported Platinum Single-Atom and Pseudo-Single-Atom Catalysts for Chemoselective Hydrogenation of Functionalized Nitroarenes. *Nat. Commun.* **2014**, *5*, 5634.
- (24) Häkkinen, H.; Abbet, S.; Sanchez, A.; Heiz, U.; Landman, U. Structural, Electronic, and Impurity-Doping Effects in Nanoscale Chemistry: Supported Gold Nanoclusters. *Angew. Chem., Int. Ed.* **2003**, *42*, 1297–1300.
- (25) Enache, D. I.; Edwards, J. K.; Landon, P.; Solsona-Espriu, B.; Carley, A. F.; Herzing, A. A.; Watanabe, M.; Kiely, C. J.; Knight, D. W.; Hutchings, G. J. Solvent-Free Oxidation of Primary Alcohols to Aldehydes Using Au-Pd/TiO<sub>2</sub> Catalysts. *Science* **2006**, *311*, 362–365.
- (26) Wu, Y.; Cai, S.; Wang, D.; He, W.; Li, Y. Syntheses of Water-Soluble Octahedral, Truncated Octahedral, and Cubic Pt–Ni Nanocrystals and Their Structure–Activity Study in Model Hydrogenation Reactions. *J. Am. Chem. Soc.* **2012**, *134*, 8975–8981.
- (27) Sheth, P. A.; Neurock, M.; Smith, C. M. First-Principles Analysis of the Effects of Alloying Pd with Ag for the Catalytic Hydrogenation of Acetylene-Ethylene Mixtures. *J. Phys. Chem. B* **2005**, *109*, 12449–12466.

- (28) Nakamura, I.; Yamanoi, Y.; Imaoka, T.; Yamamoto, K.; Nishihara, H. A Uniform Bimetallic Rhodium/Iron Nanoparticle Catalyst for the Hydrogenation of Olefins and Nitroarenes. *Angew. Chem., Int. Ed.* **2011**, *50*, 5830–5833.
- (29) Woodland, A. B.; O'Neill, H. St. C. Thermodynamic Data for Fe-bearing Phases Obtained using Noble Metal Alloys as Redox Sensors. *Geochim. Cosmochim. Acta* **1997**, *61*, 4359–4366.
- (30) Musić, S.; Filipović-Vinceković, N.; Sekovanić, L. Precipitation of Amorphous SiO<sub>2</sub> Particles and Their Properties. *Braz. J. Chem. Eng.* **2011**, *28*, 89–94.
- (31) Israelachvili, J. N.; Mitchell, D. J.; Ninham, B. W. Theory of Self-Assembly of Hydrocarbon Amphiphiles into Micelles and Bilayers. *J. Chem. Soc., Faraday Trans. 2* **1976**, *72*, 1525–1568.
- (32) Israelachvili, J. N.; Mitchell, D. J.; Ninham, B. W. Theory of Self-Assembly of Lipid Bilayers and Vesicles. *Biochim. Biophys. Acta, Biomembr.* **1977**, *470*, 185–201.
- (33) Israelachvili, J. N.; Marcelja, S.; Horn, R. G. Physical Principles of Membrane Organization. *Q. Rev. Biophys.* **1980**, *13*, 121–200.
- (34) Periasamy, M.; Thirumalaikumar, M. Methods of Enhancement of Reactivity and Selectivity of Sodium Borohydride for Applications in Organic Synthesis. *J. Organomet. Chem.* **2000**, *609*, 137–151.
- (35) Morales, F. M.; González, D.; Lozano, J. G.; García, R.; Hauguth-Frank, S.; Lebedev, V.; Cimalla, V.; Ambacher, O. Determination of the Composition of In<sub>x</sub>Ga<sub>1-x</sub>N from Strain Measurements. *Acta Mater.* **2009**, *57*, 5681–5692.
- (36) Corma, A.; Serna, P.; Calvino, J. J. Transforming Nonselective into Chemoselective Metal Catalysts for the Hydrogenation of Substituted Nitroaromatics. *J. Am. Chem. Soc.* **2008**, *130*, 8748–8753.
- (37) Zhao, K. F.; Qiao, B. T.; Wang, J. H.; Zhang, Y. J.; Zhang, T. A Highly Active and Sintering-Resistant Au/FeO<sub>x</sub>-Hydroxyapatite Catalyst for CO Oxidation. *Chem. Commun.* **2011**, *47*, 1779–1781.
- (38) Liu, L.; Qiao, B.; Chen, Z.; Zhang, J.; Deng, Y. Novel Chemoselective Hydrogenation of Aromatic Nitro Compounds over Ferric Hydroxide Supported Nanocluster Gold in the Presence of CO and H<sub>2</sub>O. *Chem. Commun.* **2009**, 653–655.
- (39) Shimizu, K. I.; Miyamoto, Y.; Kawasaki, T.; Tanji, T.; Tai, Y.; Satsuma, A. Chemoselective Hydrogenation of Nitroaromatics by Supported Gold Catalysts: Mechanistic Reasons of Size- and Support-Dependent Activity and Selectivity. *J. Phys. Chem. C* **2009**, *113*, 17803–17810.